INORGANIC CHEMISTRY FRONTIERS

RESEARCH ARTICLE

View Article Online
View Journal | View Issue

Cite this: *Inorg. Chem. Front.*, 2025, **12**, 4691

Enhancing upconversion luminescence *via* intermediate state in double perovskite phosphor: three-mode optical thermometry with python-assisted validation†

Ruitong Song, [a] Sen Yan,[a] Shihao Duan,[a] Xin Yang,[a] Esmond A. Balfour[b] and Hao Fu *[a]

High luminescence intensity, multiple modes, and high sensitivity are critical to achieving high measurement accuracy for optical thermometry in microelectronic devices and biological systems. The double perovskite phosphor, $Ca_2Sc_{0.63}Mg_{0.07}SbO_6$:$Yb^{3+}$,$Er^{3+}$, proves to be promising in overcoming these challenges. A simple high-temperature solid-phase method was used to prepare this sample which was found to exhibit red anti-Stokes luminescence under 980 nm excitation. Heterovalent substitution of Mg^{2+} for Sc^{3+} leads to lattice shrinkage and oxygen vacancy content enhancement. The induced generation of the intermediate state by the oxygen vacancy is significantly increased. This consequently enhances the upconversion luminescence intensity. The $Ca_2Sc_{0.63}Mg_{0.07}SbO_6$:$Yb^{3+}$,$Er^{3+}$ phosphor is capable of three-mode optical thermometry by thermally coupled energy states (TCES), non-thermally coupled energy states (NTCES), and CIE chromaticity shift. The NTCES-based mode has a notable relative sensitivity of $S_{r\text{-}max}$ = 4.8% K^{-1} and superior signal resolution δT = 0.016 K. Furthermore, the NTCES-based model was tested for practical applications, and the difference between the predicted theoretical temperature and the actual test temperature was kept within 6 K after about 100 000 evaluations *via* Python assistance.

Received 25th February 2025,
Accepted 13th April 2025

DOI: 10.1039/d5qi00572h

rsc.li/frontiers-inorganic

1. Introduction

High-sensitivity and reliable temperature measurement plays an important role in life, production, and technology.[1–3] Conventional contact thermometers are limited in their capabilities. They do not work properly in humid, highly corrosive, and other extreme environments because they direct contact with the objects whose temperatures are to be measured.[4,5] This has led to the emergence of various non-contact thermometry methods. In light of this, optical thermometry, which relies on the thermal response spectral properties of luminescent materials, has aroused immense interest due to its advantages of real-time feedback, high spatial, and thermal resolutions.[6–8] Particularly, the concept of self-calibration has recently become a hot research topic. The method is highly resistant to external disturbances, such as fluctuations in sample concentration, fluctuations in excitation power, and other factors including those affecting the absolute intensity.[9,10] Optical thermometry relies on temperature-sensitive properties such as luminescence intensity ratio (LIR), excitation intensity ratio, lifetime, Commission Internationale de L'Eclairage (CIE), and bandwidth.[11–15] For self-calibration and multimode operation, the material needs to possess all these temperature-sensitive properties. This is necessary to avoid temperature measurement inaccuracies that may be caused by a single mode.

Upconversion (UC) luminescent materials are well known for their potential applications in biomedical imaging, solar cells, and optical anti-counterfeiting.[16–19] Also, due to the unique optical properties of visible light generated by near-infrared excitation, UC luminescent materials are promising candidates for optical thermometry. Abundant energy states and suitable thermally coupled energy states (TCES) in Er^{3+} make it a desirable UC luminescent center for optical thermometry. Although optical thermometry in different Er^{3+}-doped materials based on TCES or/and non-thermally coupled energy states (NTCES) have been extensively studied,[20–22] it is of utmost interest to explore Er^{3+}-activated materials utilizing multifunctional thermometry techniques. The 4f–4f transition prohibited for Er^{3+} ions leads to the small absorption cross-section at 980 nm and low UC luminescence intensity. Yb^{3+}

[a]*School of Physics, University of Electronic Science and Technology of China, Chengdu 611731, China. E-mail: fuhao@uestc.edu.cn*
[b]*School of Physical Sciences, C. K. Tedam University of Technology and Applied Sciences, Navrongo, Ghana*

† Electronic supplementary information (ESI) available. See DOI: https://doi.org/10.1039/d5qi00572h

ion has been utilized as a sensitizer due to its large absorption cross-section (980 nm), resulting in effective enhancement of luminescence intensity.[23,24] However, further, enhancing UC luminescence intensity based on Yb^{3+}/Er^{3+} co-doping remains a significant challenge. Yet, improving UC luminescence intensity is important as it affects optical thermometry directly. Enhancement of UC luminescence intensity is commonly achieved by doping with alkali metal ions, alkaline earth metal ions, or transition metal ions through mechanisms like change in lattice parameters, concentration quenching, or oxygen vacancy.[25–30] Amongst these mechanisms, though the presence of oxygen vacancy is known to enhance UC luminescence, its exact role played remains ambiguous. Oxygen vacancy plays a very important role in enhancing the photocatalytic performance in the photocatalytic field.[31–33] Liang *et al*. achieved NIR-driven CO_2 overall splitting by introducing the intermediate band to collect near-infrared light through the oxygen vacancy.[34] Li *et al*. proposed the introduction of an intermediate band to enhance the UC luminescence and achieved good photocatalytic performance.[35] However, the origin and mechanism of enhancement of UC luminescence by oxygen vacancy remains yet to be solved with direct experimental evidence.

It is noteworthy that in the field of luminescence, $A_2B'B''O_6$ double perovskite is commonly regarded as an ideal host material due to the rich octahedral environment and high chemical stability.[36–38] Again, to realize improved luminescence properties, appropriate crystal field environment is required as well as suitable sites to accommodate the luminescent centers.

Herein, the double perovskite phosphor $Ca_2Sc_{0.63}Mg_{0.07}SbO_6$:$Yb^{3+}$,$Er^{3+}$ is designed to enhance UC luminescence intensity and employed in three-mode optical thermometry. Heterovalent substitution of Mg^{2+} for Sc^{3+} leads to lattice shrinkage and increase in oxygen vacancy content. We show that the oxygen vacancy-induced generation of intermediate state results in the UC luminescence intensity enhancement and provide direct evidence for the existence of the intermediate state. The intrinsic process mechanism is explained. Self-calibration and multimode optical thermometry are realized by three thermometry modes: TCES, NTCES, and CIE chromaticity shift. The NTCES-based mode shows outstanding relative sensitivity and superior signal resolution. In addition, the reliability of this phosphor in practical applications is further evaluated by Python assistance.

2. Experimental

2.1. Preparation

The raw materials include Yb_2O_3 (99.99%), Er_2O_3 (99.99%), Sc_2O_3 (99.9%), $CaCO_3$ (99%), Sb_2O_5 (99%) and MgO (99%). The above weighed raw materials were mixed in an agate mortar and ground for 30 minutes and then sintered in a muffle furnace at 1500 °C for 6 h and cooled naturally to room temperature. Finally, the products were obtained after grinding into homogeneous particles. The reducing atmosphere is a mixture of 95% N_2 and 5% H_2 that is kept at 1000 °C for 200 minutes and then naturally cooled to room temperature.

2.2. Characterization

A DX-2700 diffractometer was used to collect X-ray diffraction (XRD) patterns for all samples. The Rietveld refinement was performed with the General Structure Analysis System (GSAS) software. A Nova NanoSEM 450 scanning electron microscope (SEM) was used to characterize the morphology of the sample with the accelerating voltage of 20 kV, and an energy dispersive spectrometer (EDS) was used to measure the elemental compositions. The powder samples were first uniformly dispersed on a conductive adhesive and then coated with a gold film on the surface. The diffuse reflectance spectra of the samples were measured by a Hitachi 4100 spectrometer. The optical properties of the samples including UC spectra were measured at different temperatures using an Edinburgh FLS1000 spectrometer with a 980 nm excitation source. For the upconversion spectra test, we used a suitable filter (850 nm) to separate the upconversion light from the diffraction grating with higher-order peaks. To ensure the accuracy of our experimental results, we carefully control external factors by using a stable excitation light source to maintain consistent excitation intensity and calibrating the detection system to minimize instrumental errors. In addition, we ensured that all measurement samples were prepared and tested under identical conditions to eliminate errors due to sample differences. Electron paramagnetic resonance (EPR) curves were recorded using a Bruker EMX Plus spectrometer and all other conditions were constant for two samples of undoped/doped Mg^{2+}. The actual temperature is obtained using an infrared thermometer DLX-HC2508. Python is used as the computer programming language.

3. Results and discussion

3.1. Structural and morphological analysis

The XRD patterns of $Ca_2Sc_{0.9-x}SbO_6$:$0.1Yb^{3+}$,xEr^{3+} ($0.01 \le x \le 0.09$) and $Ca_2Sc_{0.95-y}SbO_6$:$0.05Er^{3+}$,yYb^{3+} ($0.05 \le y \le 0.3$) phosphors are shown in Fig. S1a and b.† The reflection peaks are consistent with those of the XRD pattern of Ca_2ScSbO_6 (ICSD#262995). The Yb^{3+}/Er^{3+} doping thus maintains the Ca_2ScSbO_6 structure without introducing a new impurity phase. Since Yb^{3+}/Er^{3+} are close to Sc^{3+} in valence and ionic radius [CN = 6, $r(Sc^{3+})$ = 0.745 Å, $r(Yb^{3+})$ = 0.868 Å, $r(Er^{3+})$ = 0.89 Å],[39] they are likely to displace Sc^{3+} site. Table S1† provides detailed results of the structure refinement, and the concentration of Yb^{3+} (0.2243) is very close to the designed doping concentration (0.25), which confirms that they replace the Sc^{3+} site. Fig. S2† shows the refinement result for optimal Yb^{3+}/Er^{3+} doping. The low residuals indicate that the compound indeed crystallizes in a pure phase single phase. Fig. 1a exhibits the XRD patterns of $Ca_2Sc_{0.7-z}Mg_zSbO_6$:$0.25Yb^{3+}$,$0.05Er^{3+}$ with z in the interval of $0.01 \le z \le 0.15$. It can be observed that all the samples remain in pure single phase after doping with Mg^{2+}.

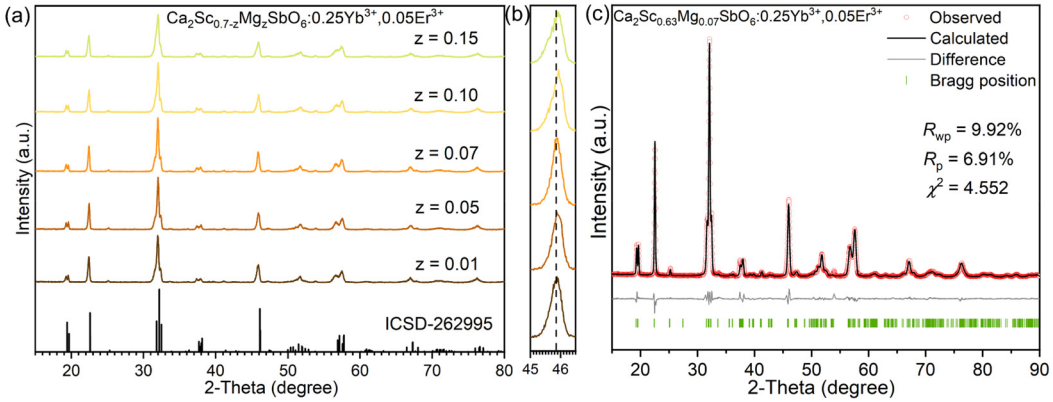

Fig. 1 (a) XRD patterns and (b) the magnified diffraction peak at the 45.9° of the $Ca_2Sc_{0.7-z}Mg_zSbO_6$:0.25Yb^{3+},0.05Er^{3+}. (c) Rietveld refinement of $Ca_2Sc_{0.63}Mg_{0.07}SbO_6$:0.25Yb^{3+},0.05Er^{3+}.

Generally, Mg^{2+} would be expected to replace the alkaline earth metal Ca^{2+} of the same main group. However, considering the significant difference in ionic radii, [*e.g.*, CN = 6, $r(Ca^{2+})$ = 1 Å, $r(Sc^{3+})$ = 0.745 Å, $r(Mg^{2+})$ = 0.72 Å],[39] the Mg^{2+} is rather more inclined to displace Sc^{3+} with comparable ionic radius. In Fig. 1b, the diffraction peak located at 45.9° shifts towards the right with increasing Mg^{2+} doping, which proves the replacement of Mg^{2+} for Sc^{3+}. The ionic radius of Mg^{2+} being smaller than that of Sc^{3+}, results in the diffraction peak showing a shift to higher angles. Moreover, even when the doping concentration of Mg^{2+} reaches 0.07, the shift of the diffraction peak remains insignificant, a phenomenon that coincides with the fact that the ionic radii of Mg^{2+} and Sc^{3+} are very close, and thus Mg^{2+} prefers to substitute for Sc^{3+} rather than Ca^{2+}. As the Mg^{2+} doping concentration continues to increase, the diffraction peak shift becomes more obvious. Tables S1 and S2† provide detailed structural refinement results for the Mg^{2+} undoped and the representative Mg^{2+} doped $Ca_2Sc_{0.63}Mg_{0.07}SbO_6$:0.25Yb^{3+},0.05Er^{3+} samples, respectively. The Rietveld refinement of the $Ca_2Sc_{0.63}Mg_{0.07}SbO_6$:0.25Yb^{3+},0.05Er^{3+} is shown in Fig. 1c. Results in Tables S1 and S2† show shrinkage of the unit cell after substitution by the Mg^{2+} ions. The cell parameters *a*, *b*, *c*, and volume *V* decrease for the Mg^{2+} ions doped sample. This is consistent with the shift in peak position in Fig. 1b. In addition, if Mg^{2+} is set to replace the Ca^{2+} position, the occupation of the refinement result is negative, which is wrong, indicating that Mg^{2+} cannot replace the Ca^{2+} position. While setting Mg^{2+} to replace the Sc^{3+} position, the occupation of the refined result (0.0608) is very close to the design doping (0.07) (Table S2†). Therefore, as a consequence of the Mg^{2+} ion doping, Mg^{2+} occupies the Sc^{3+} 2d site. Moreover, although oxygen vacancy is present in the Mg^{2+} undoped sample, it increases in content after doping. Structural alterations often cause changes in the optical properties of materials. The substitution of Mg^{2+} for Sc^{3+} is usually accompanied by the formation of oxygen vacancies (V_O) in order to maintain charge neutrality due to the lower valence state of Mg^{2+} compared to Sc^{3+}. Therefore, the content of oxygen vacancy increases after doping Mg^{2+}. The SEM image, EDS, and element mapping of the $Ca_2Sc_{0.63}Mg_{0.07}SbO_6$:0.25Yb^{3+},0.05Er^{3+} phosphor are shown in Fig. S3a–c.† The sample exhibits agglomeration, which may be attributed to high-temperature sintering.[40] In addition, some holes can be observed, caused by escaping gas during sintering.[41] The seven elements Ca, Sc, Sb, O, Mg, Yb, and Er are homogeneously distributed in the synthesized sample, as shown in the EDS and elemental mapping images.

3.2. Luminescent properties

To obtain the optimal UC luminescence performance, Ca_2ScSbO_6 samples doped with different concentrations of Yb^{3+} and Er^{3+} were prepared. Under 980 nm excitation, all the samples show a distinct red emission band and two weak green bands, including an intense red UC belonging to the $^4F_{9/2} \rightarrow {}^4I_{15/2}$ transition at 662 nm as shown in Fig. S4a and b.† The two weak green ones are located at 528 and 548 nm for the $^2H_{11/2} \rightarrow {}^4I_{15/2}$ and $^4S_{3/2} \rightarrow {}^4I_{15/2}$ transitions, respectively. The variation of Er^{3+} and Yb^{3+} doping concentrations hardly affects the position of the emission bands. However, with the increase in Er^{3+} and Yb^{3+} concentrations, the UC luminescence intensity changed remarkably to reach maxima at x = 0.05 and y = 0.25, respectively, and then decreased due to concentration quenching.[42–44] Therefore, the optimal composition in terms of the UC luminescence intensity is $Ca_2Sc_{0.7}SbO_6$:0.25Yb^{3+},0.05Er^{3+}. To further enhance the UC luminescence intensity, Mg^{2+} ions are introduced for co-doping based on Yb^{3+}/Er^{3+} doping. As depicted in Fig. 2a, the UC luminescence intensity reaches its strongest (4.32 times higher than that of the undoped) with increased Mg^{2+} doping. However, the UC luminescence intensity shows a decreasing trend with Mg doping greater than 0.07. Moreover, to further verify the effect of oxygen vacancy content, we annealed the optimal sample under reductive atmosphere treatment. As shown in Fig. S5,† the UC luminescence intensity of the optimal sample after annealing under reducing atmosphere is substantially weakened and the color of the sample changes from white to gray. Since doping Mg^{2+} to replace Sc^{3+} leads to charge imbalance due to valence difference, oxygen vacancy

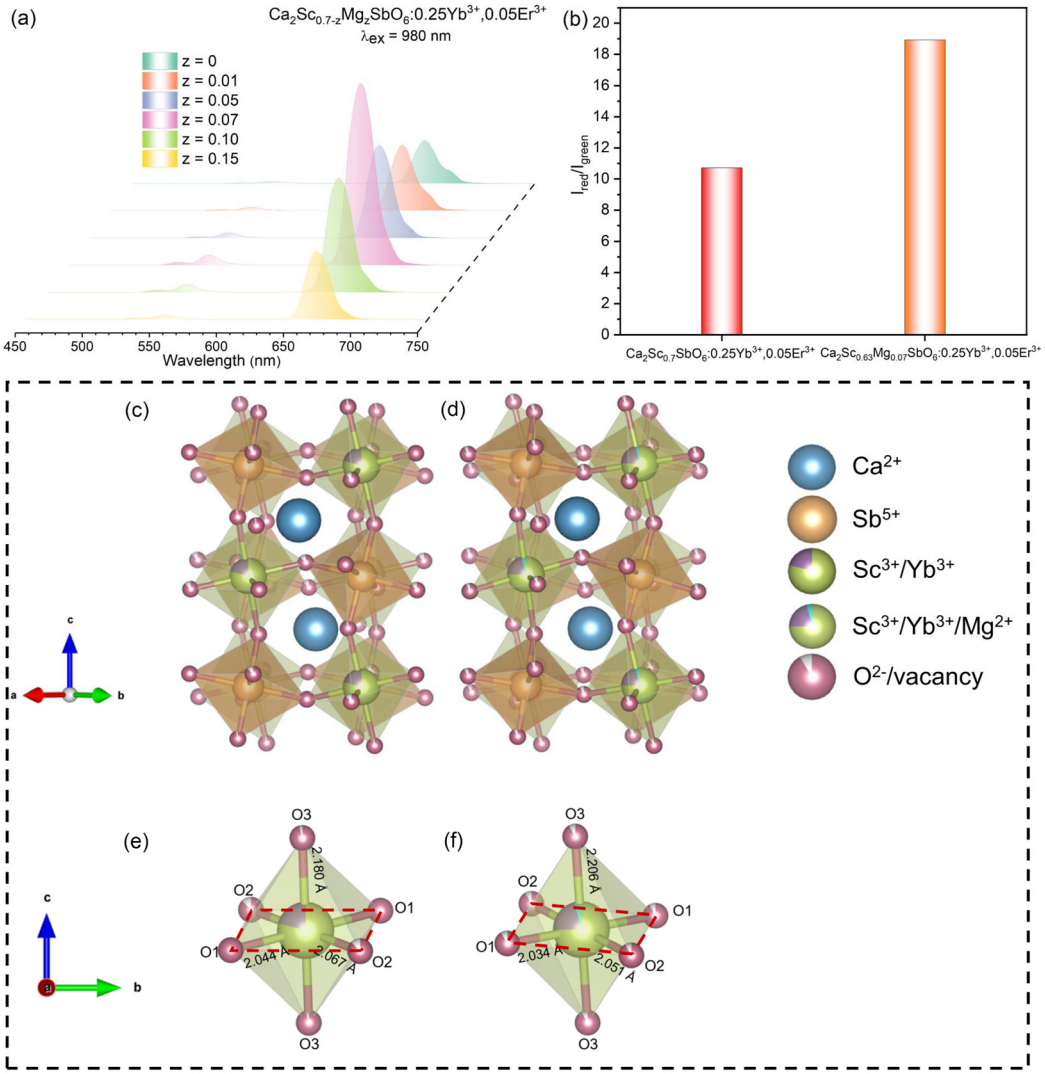

Fig. 2 (a) UC spectra of $Ca_2Sc_{0.7-z}Mg_zSbO_6$:0.25Yb^{3+},0.05Er^{3+} (z = 0–0.15) under 980 nm laser excitation. (b) Red–green integrated intensity ratio of $Ca_2Sc_{0.7}SbO_6$:0.25Yb^{3+},0.05Er^{3+} and $Ca_2Sc_{0.63}Mg_{0.07}SbO_6$:0.25$Yb^{3+}$,0.05$Er^{3+}$. Crystal structure of (c) $Ca_2Sc_{0.7}SbO_6$:0.25Yb^{3+},0.05Er^{3+} and (d) $Ca_2Sc_{0.63}Mg_{0.07}SbO_6$:0.25$Yb^{3+}$,0.05$Er^{3+}$. Schematic diagram of sublattice distortion caused by (e) undoped and (f) doped Mg^{2+}.

(V_O) is formed in the sample to maintain the electrical neutrality of the lattice. Therefore, this suggests that a moderate amount of oxygen vacancies can enhance the UC luminescence intensity, while an excess of oxygen vacancies can weaken it. This is because oxygen vacancies, as a type of defect, when present in excess, act as quenching centers that continuously absorb photons, which then leads to an increase in the harmful nonradiative relaxation of the Er^{3+} excited state, thus quenching upconversion luminescence. In addition, the calculated red-to-green integrated intensity ratio in Fig. 2b indicates a significant increase in the ratio from 10.7 to 18.9 for Mg^{2+} doping of z = 0.07. The UC luminescence spectra were further analyzed under different laser power pumping. This is shown in Fig. S6a and c.† The linear fitting of the bi-logarithmic graph of UC intensity and pumping power, according to eqn (S1)† gives the value of the photon number n. From Fig. S6b,† the slopes (n) of undoped Mg^{2+} at 528, 548, and 662 nm are 1.80, 1.70, and 1.49, respectively, indicating that the green UC luminescence is both two-photon processes, whereas the red UC emission may be a mix of single-photon and two-photon processes. However, from Fig. S6d,† upon doping with Mg^{2+}, the increased slopes (n) of 2.15, 2.13, and 1.85 are obtained for the same respective pumping powers of 528, 548, and 662 nm. The slopes of the 528 and 548 nm pump powers are both slightly greater than 2, which means that they are still two-photon processes, whereas the red UC process completely changes to a two-photon process. Therefore, by doping with Mg^{2+} ions, the red UC luminescence intensity is enhanced more obviously, which corresponds well to the red–green ratio enhancement in Fig. 2(b).

Coupled with the previous Rietveld refinement result analysis above for the Mg^{2+} doped sample, the oxygen vacancy content is significantly increased after doping with Mg^{2+}. In addition, shrinkage of the cell parameters (a, b, c, and V) after

the Mg^{2+} doping indicates a change in the crystal field. Fig. 2c and d show schematic diagrams of the crystal structures of the Mg^{2+} undoped and Mg^{2+} doped samples. The Mg^{2+} undoped and Mg^{2+} doped polyhedra are drawn separately in Fig. 2e and f. The structure undergoes a slight distortion (see red dashed parallelogram in Fig. 2e and f) after doping with Mg^{2+}. The substitution of Mg^{2+} for Sc^{3+} leads to changes in the lengths of the Sc–O bonds. The bond lengths of Sc–O1, O2, and O3 are 2.044, 2.067, and 2.180 Å, respectively for the Mg^{2+} undoped sample, while the bond lengths of Sc–O1 and O2 are shortened to 2.034 Å and 2.051 Å, respectively with that of Sc–O3 increased to 2.206 Å for the Mg^{2+} doped sample. Consequently, the polyhedra are contracted horizontally, and stretched vertically to become slender. Therefore, the lattice contraction and oxygen vacancy may be responsible for the enhanced UC luminescence intensity and the larger *n* value.

The diffuse reflectance spectra, bandgap, and EPR curves of both Mg^{2+} undoped and doped samples were tested. The results are shown in Fig. 3a–d. In Fig. 3a, many characteristic absorption peaks of Er^{3+} and Yb^{3+} occur. Peaks located at 379 ($^4I_{15/2} \rightarrow {}^4G_{11/2}$), 491 ($^4I_{15/2} \rightarrow {}^4F_{7/2}$), 522 ($^4I_{15/2} \rightarrow {}^2H_{11/2}$), 546 ($^4I_{15/2} \rightarrow {}^4S_{3/2}$), 658 ($^4I_{15/2} \rightarrow {}^4F_{9/2}$), and 801 ($^4I_{15/2} \rightarrow {}^4I_{9/2}$) nm, respectively, belong to Er^{3+} and the broad absorption band located at 980 nm is attributed to the transitions of Er^{3+} ($^4I_{15/2} \rightarrow {}^4I_{11/2}$) and Yb^{3+} ($^2F_{7/2} \rightarrow {}^2F_{5/2}$). The absorption peaks are enhanced after doping with Mg^{2+}. Surprisingly, two new absorption peaks at 1116 and 1160 nm appear after Mg^{2+} doping. For comparison, we also tested the diffuse reflectance spectrum of Ca_2ScSbO_6, as shown in Fig. S7,† which does not show any absorption peaks at these two positions. They are new energy states (intermediate states) induced by the formation of oxygen vacancy generated by the heterovalent substitution of Mg^{2+} for Sc^{3+}. In 2018, Liang *et al.* revealed through theoretical calculations that oxygen vacancy reaching a critical density results in the formation of an intermediate band,[34] but direct experimental evidence on the intermediate band is not yet directly available. So, this could be the reason for the enhanced UC luminescence intensity. The higher oxygen vacancy content after Mg^{2+} doping, confirmed by Rietveld refinement (Tables S1 and S2†), strongly confirms this. The EPR curve is a well-known method for detecting the presence of oxygen vacancy.[45] To further demonstrate the increase in oxygen vacancy content, the EPR curves of the Mg^{2+} undoped and Mg^{2+} doped samples were obtained under the same conditions, as shown in Fig. 3c. The signal intensity of the Mg^{2+} doped sample is much stronger than that of the non-Mg^{2+} doped (g = 2.004). This reflects their difference in oxygen vacancy content and is consistent with the Rietveld refinement results and diffuse reflectance spectra. In addition, the bandgaps of the undoped and doped Mg^{2+} samples were calculated (using eqn (S2) and (S3)†) to be 4.30 and 4.26 eV, respectively, as shown in Fig. 3b and d. It is evident that the Mg^{2+} doping decreases the bandgap from 4.30 eV to 4.26 eV. Also, the presence of oxygen vacancy shifts the oxide Fermi energy level upward, leading to the emergence of a defect energy state (the intermediate state) in the bandgap, thus reducing the width of the energy band.[46,47] This establishes that indeed oxygen vacancy induces the intermediate state that drives the appearance of new absorption peaks in the diffuse reflectance spectra.

On the basis of these results, a mechanism is proposed as shown in Fig. 3e. Under the excitation of 980 nm laser, the Yb^{3+} ions in the ground state ($^2F_{7/2}$) are pumped to the excited state ($^2F_{5/2}$). The excited Yb^{3+} ions relax back to the ground state by non-radiative relaxation. This transfers energy to the nearby Er^{3+} ions, exciting them from the $^4I_{15/2}$ ground state to $^4I_{11/2}$ excited state by ground state absorption (GSA). Subsequently, the $^4I_{11/2}$ state excited Er^{3+} ions, through energy transfer (ET) from the $^2F_{5/2}$ excited Yb^{3+} ions state, are further excited to the higher $^4F_{7/2}$ state *via* excited state absorption 1 (ESA1). Otherwise, the Er^{3+} ions at the $^4I_{11/2}$ state relaxes to the $^4I_{13/2}$ energy state *via* multi-phonon relaxation (MPR). Through MPR, the Er^{3+} ions in the excited $^4F_{7/2}$ state quickly fall to the $^2H_{11/2}$ and then to the $^4S_{3/2}$ states. Eventually, the Er^{3+} ions in the $^2H_{11/2}$ and $^4S_{3/2}$ states return to the ground $^4I_{15/2}$ state by radiative transition, producing two green emissions at 528 and 548 nm respectively. This is consistent with the power-dependent results of the 528, 548 nm in Fig. S6(d),† which the *n* values are 2.15 and 2.13, respectively, and both are two-photon processes, *i.e.*, both green emissions go through both GSA and ESA1 processes. On the other hand, two pathways exist for red emission. The Er^{3+} ions at the $^4S_{3/2}$ state undergo MPR to the $^4F_{9/2}$ state before returning to the ground $^4I_{15/2}$ state by the radiative transition to produce red emission. Alternatively, Er^{3+} ions located in the $^4I_{13/2}$ state, are excited to the $^4F_{9/2}$ through ESA2. This is then followed by deexcitation to the ground $^4I_{15/2}$ state by the radiative transition to produce red emission. This is also consistent with the power-dependent test result of 662 nm in Fig. S6(d),† which has an *n* value of 1.85 for a two-photon process, *i.e.*, the red emission undergoes both GSA and ESA2 processes. It is worth noting that the intermediate state contributes significantly to the enhancement of UC luminescence intensity. Since the intermediate states are at lower energies (1116 and 1160 nm) than the 980 nm laser, the 980 nm laser can excite electrons from the valence band to the intermediate state directly, thus resulting in two ET pathways. In addition, due to the generation of localized lattice distortions that enhance electroacoustic coupling and promote phonon-assisted processes, which enables energy transfer from the intermediate state to the Yb^{3+} $^2F_{5/2}$ excited state and the Er^{3+} $^4I_{11/2}$ excited state. One path is the transfer of the electrons at the intermediate state to the Yb^{3+} $^2F_{5/2}$ excited state. The second path constitutes the transfer of electrons at the intermediate state to the Er^{3+} $^4I_{11/2}$ excited state. The two pathways result in an increase in the populations of the Er^{3+} ion $^2H_{11/2}$, $^4S_{3/2}$, and $^4F_{9/2}$ states causing enhancement of the green and red UC luminescence.

3.3. Three-mode optical thermometry

Two- and three-dimensional temperature-dependent emission spectra of $Ca_2Sc_{0.63}Mg_{0.07}SbO_6$:0.25$Yb^{3+}$,0.05$Er^{3+}$ sample for the temperature range from 298 to 573 K are shown in Fig. 4a.

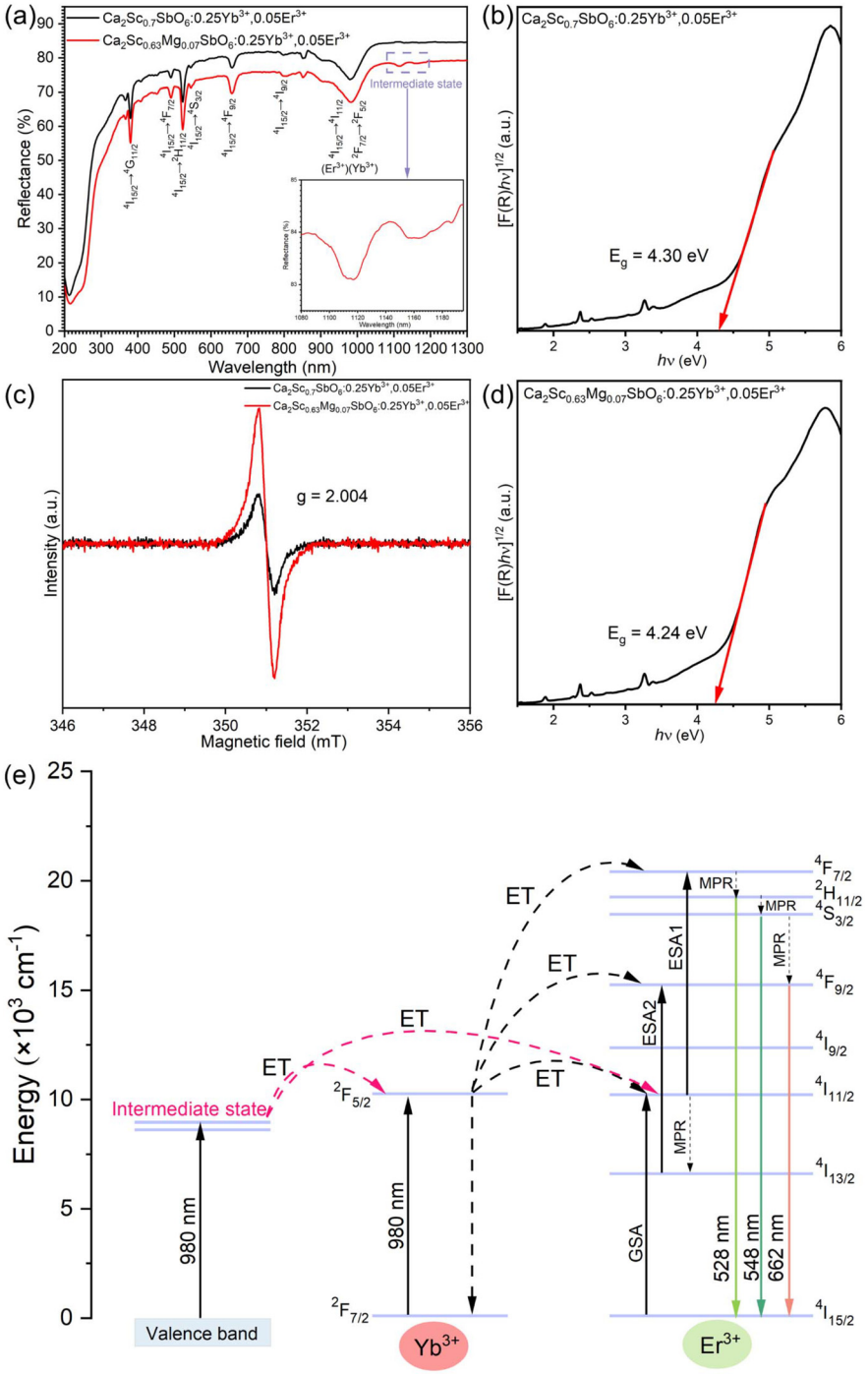

Fig. 3 (a) Diffuse reflectance spectra and (c) EPR curves of $Ca_2Sc_{0.7}SbO_6$:0.25Yb^{3+},0.05Er^{3+} and $Ca_2Sc_{0.63}Mg_{0.07}SbO_6$:0.25$Yb^{3+}$,0.05$Er^{3+}$. Bandgap plots of (b) $Ca_2Sc_{0.7}SbO_6$:0.25Yb^{3+},0.05Er^{3+} and (d) $Ca_2Sc_{0.63}Mg_{0.07}SbO_6$:0.25$Yb^{3+}$,0.05$Er^{3+}$. (e) Schematic diagram and the possible UC mechanism.

The intensity of the peak located at 528 nm increases with temperature in the range from 298 to 498 K but decreases with temperature in the range from 498 to 573 K. In Fig. 4b, the intensity decreases monotonically with temperature for the peak located at 548 nm. This phenomenon can be attributed to the narrow energy gap between the $^4S_{3/2}$ and $^2H_{11/2}$ energy states, which belong to the TCES. The proximity of the two states allows the $^2H_{11/2}$ state to easily be occupied by electrons from the $^4S_{3/2}$ state through thermal excitation.[48] The different responses of the two green UC emissions to temperature are useful in optical thermometry. The plot of LIR (I_{528}/I_{548}) against the temperature curve shown in Fig. 4c was fitted using eqn (S4)† (the two energy states obey the Boltzmann distribution). The R^2 value of 0.999 for the curve fitting, indicates good agreement of the data with eqn (S4).† The absolute sensitivity (S_a) and relative sensitivity (S_r) are important metrics for

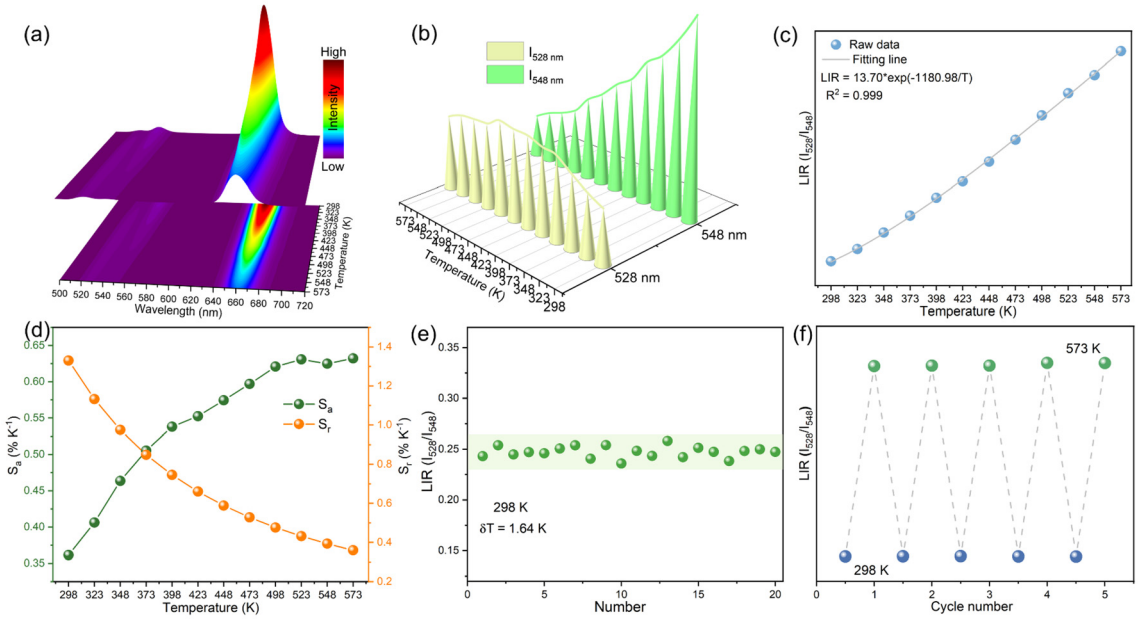

Fig. 4 (a) Two- and three-dimensional temperature-dependent emission spectra of $Ca_2Sc_{0.63}Mg_{0.07}SbO_6$:0.25$Yb^{3+}$,0.05$Er^{3+}$. (b) Intensities of 528 nm and 548 nm *versus* temperature. (c) LIR (I_{528}/I_{548}) *versus* temperature. (d) S_a and S_r *versus* temperature. (e) Twenty measurements of LIR (I_{528}/I_{548}) and calculated temperature resolution δT at 298 K. (f) Repeatability of LIR (I_{528}/I_{548}) for 298 and 573 K.

evaluating the performance of optical thermometry given by the eqn (S5) and (S6).† As depicted in Fig. 4d, the maximum $S_{a\text{-}max}$ at 573 K is 0.63% K^{-1}, and the maximum $S_{r\text{-}max}$ at 298 K is 1.33% K^{-1}. To determine the smallest temperature change that can be resolved by the LIR sensor, the temperature resolution (δT) is evaluated. It is strongly dependent on the LIR deviation, in accordance with eqn (S7).† The optimal value of δT was determined from Fig. 4e to be 1.64 K at 298 K under the same conditions for all twenty spectral measurements. The repeatability (R) was calculated with eqn (S8)† to assess the temperature cycling behavior. From the LIR values for five consecutive cycles (Fig. 4f), the R values for 298 and 573 K were calculated to be 99.1% and 99.2%, respectively.

In Fig. S8,† the red UC intensity of the sample is significant over a wide temperature range and decreases rapidly with increasing temperature. These properties make the sample suitable for optical thermometry. Since the energy difference between the $^2H_{11/2}$ and $^4F_{9/2}$ energy states is relatively large, they are not TCESs. Boltzmann distribution can not be used to describe NCTES due to the high energy difference in the involved states. In the absence of a physical model, we use a numerical approach and fit to a polynomial. The FIR values of the NTCES can be fitted by the polynomial equation eqn (S9)† as shown in Fig. 5a. The experimental data fit well with a goodness of fit of 0.998. The corresponding relative and absolute sensitivities were calculated using eqn (S10) and (S11),† and the maximum values of both are $S_{a\text{-}max}$ = 0.17% K^{-1} and $S_{r\text{-}max}$ = 4.8% K^{-1}, respectively, as shown in Fig. 5b. In addition, its δT was evaluated according to eqn (S7),† and the optimal value of δT at 298 K was determined to be 0.016 K under the same conditions for 20 spectral measurements (Fig. 5c). It is worth mentioning that the δT value (0.016 K) is two magnitudes lower than that of 0.7 K for the cubic phase $LiLuF_4$:18%Yb^{3+}/2%Er^{3+},[49] which is also an intensity-based thermometry. Its R was also calculated using eqn (S8)† and based on the LIR values of five consecutive cycles (Fig. 5d), the R values at 298 K and 573 K were calculated to be 99.3% and 98.6%, respectively. Fig. 5e compares the $S_{r\text{-}max}$ of other Yb^{3+}/Er^{3+} co-doped LIR-based optical thermometry.[50–63] The maximum $S_{r\text{-}max}$ value of $Ca_2Sc_{0.63}Mg_{0.07}SbO_6$:0.25$Yb^{3+}$,0.05$Er^{3+}$ is much superior to those of most other materials. The $Ca_2Sc_{0.63}Mg_{0.07}SbO_6$:0.25$Yb^{3+}$,0.05$Er^{3+}$ compound is therefore an ideal LIR optical thermometry with high S_r and low δT.

To further explore the potential of using $Ca_2Sc_{0.63}Mg_{0.07}SbO_6$:0.25$Yb^{3+}$,0.05$Er^{3+}$ for temperature sensing in the NTCES mode, we developed a straightforward temperature measurement platform, as illustrated in Fig. 6a. The $Ca_2Sc_{0.63}Mg_{0.07}SbO_6$:0.25$Yb^{3+}$,0.05$Er^{3+}$ sample was placed on a heating stage and excited with a 980 nm laser. The resulting spectral data were transmitted through optical fiber to a computer, which employed the Python programming language to calculate and predict the LIR and the corresponding temperature value (T). Subsequently, the real-time temperature measured by an infrared thermometer was compared with the predicted theoretical temperature values to further evaluate the reliability of this phosphor in practical application. Fig. 6b–g presents the theoretically predicted temperatures and the actual test temperatures. After approximately 100 000 evaluations, the difference between the predicted theoretical temperature and the actual test temperature remains within 6 K. This finding indicates that the $Ca_2Sc_{0.63}Mg_{0.07}SbO_6$:0.25$Yb^{3+}$,0.05$Er^{3+}$ phosphor is a reliable

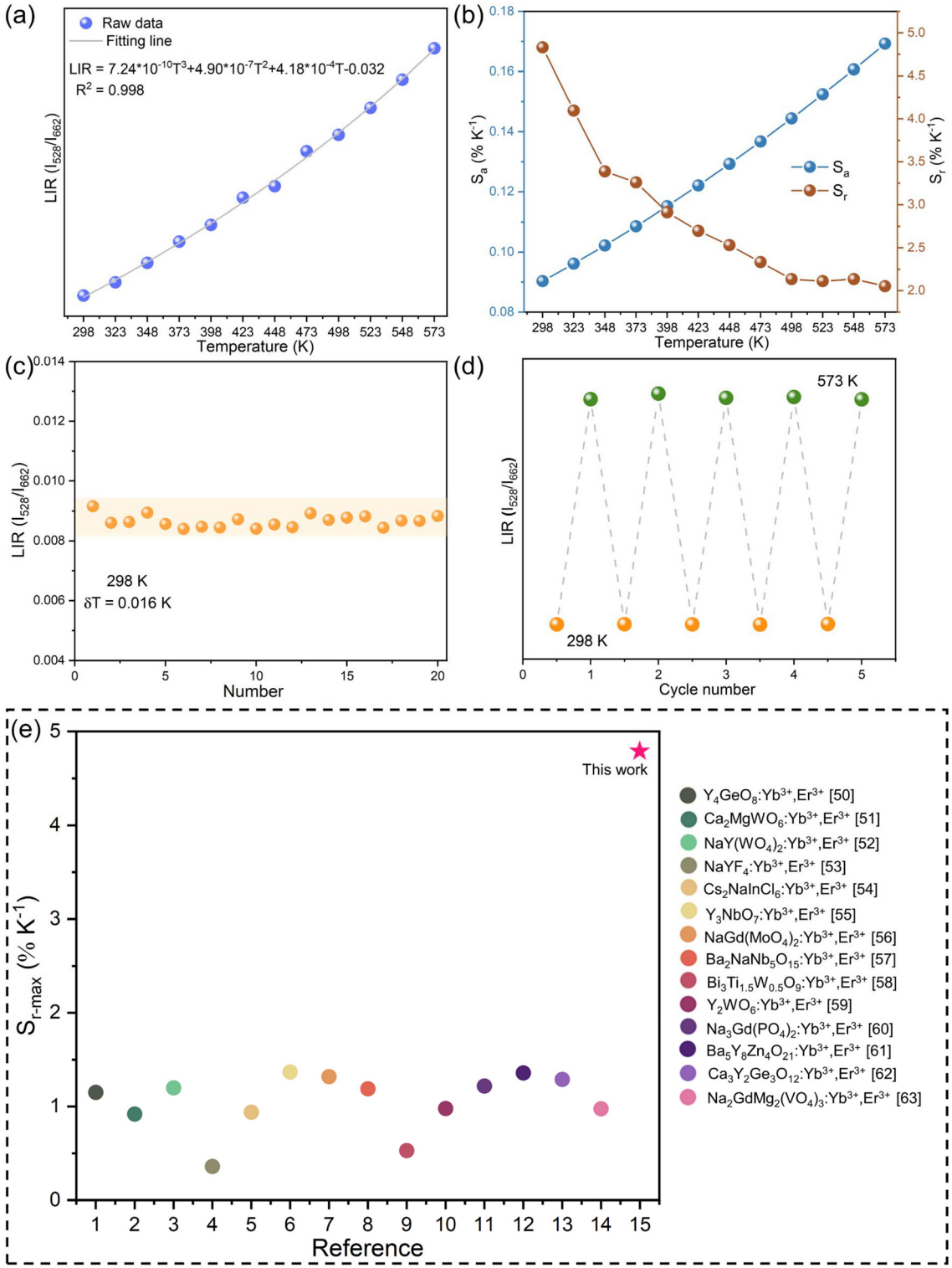

Fig. 5 (a) LIR (I_{528}/I_{662}) *versus* temperature. (b) S_a and S_r *versus* temperature. (c) Twenty measurements of LIR (I_{528}/I_{548}) and calculated temperature resolution δT at 298 K. (d) Repeatability of LIR (I_{528}/I_{548}) between 298 and 573 K. (e) Comparison of the maximum relative sensitivity of $Ca_2Sc_{0.63}Mg_{0.07}SbO_6$:0.25$Yb^{3+}$,0.05$Er^{3+}$ with those of some reported Yb^{3+},Er^{3+} co-doped samples based on LIR. Numbers in parentheses indicate references.

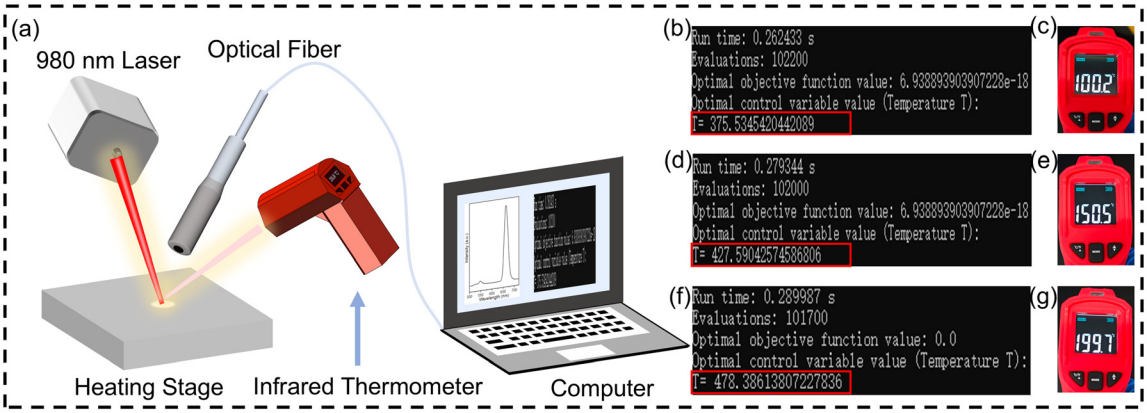

Fig. 6 (a) Experimental arrangement of temperature sensing system. (b, d and f) Theoretical temperature values calculated using spectral data and computer programming language. (c, e and g) Actual temperature values measured by infrared thermometer.

Table 1 Chromaticity shift (ΔE_s) of $Ca_2Sc_{0.63}Mg_{0.07}SbO_6$:0.25$Yb^{3+}$,0.05$Er^{3+}$ in response to temperature

Phosphor	Temperature (K)	CIE coordinates	$S_{r\text{-}max}$ (% K^{-1})	Ref.
$Al_2Mo_3O_{12}$:Ho^{3+},Yb^{3+}	323–543	*x*	0.112	64
$Al_2Mo_3O_{12}$:Ho^{3+},Yb^{3+}	323–543	*x*	0.102	64
$Sr_4Al_{14}O_{25}$:Mn^{4+},Tb^{3+}	123–573	*x*	0.6	65
$Sr_4Al_{14}O_{25}$:Mn^{4+},Tb^{3+}	123–573	*y*	0.4	65
$LaNbO_4$:Bi^{3+},Eu^{3+}	303–483	*x*	0.47	66
$LaNbO_4$:Bi^{3+},Sm^{3+}	303–483	*x*	0.36	66
$Ca_3LiZnV_3O_{12}$:Sm^{3+}	303–483	*x*	0.567	15
$Ca_2Sc_{0.63}Mg_{0.07}SbO_6$:$Yb^{3+}$,$Er^{3+}$	298–573	*y*	0.608	This work

candidate for temperature sensing. Consequently, $Ca_2Sc_{0.63}Mg_{0.07}SbO_6$:0.25$Yb^{3+}$,0.05$Er^{3+}$ phosphor emerges as a feasible, dependable, and promising optical thermometry for UC applications, providing a solid foundation for further advancements in the field of optical temperature sensors.

Owing to the different changes in red and green emissions with increasing temperature, the color of the sample changes from red to yellow, showing a significant shift in the color coordinates as shown in Fig. S9.† The color change is quantified by chromaticity shift (ΔE_s), calculated with eqn (S13).† The results are given in Table S3.† With its ΔE_s as high as 0.147 the sample has remarkable thermochromic performance and has the potential in high-temperature safety signs. Moreover, the high ΔE_s value also implies its potential application in optical thermometry. Fig. S10a† presents the fitting curve of CIEy *versus* temperature. The R^2 = 0.994 value indicates a very good agreement of the data with eqn (S12).† The S_a and S_r were also determined from eqn (S5) and (S6)† and plotted in Fig. S10b.† The results give $S_{a\text{-}max}$ and $S_{r\text{-}max}$ values of 0.229% K^{-1} (298 K) and 0.608% K^{-1} (298 K), respectively. The $S_{r\text{-}max}$ value of $Ca_2Sc_{0.63}Mg_{0.07}SbO_6$:0.25$Yb^{3+}$,0.05$Er^{3+}$ sample is superior to most optical thermometry based on CIE coordinates (see Table 1). Clearly, the $Ca_2Sc_{0.63}Mg_{0.07}SbO_6$:0.25$Yb^{3+}$,0.05$Er^{3+}$ phosphor possesses impressive UC emission characteristics and multimode temperature sensitivity based on TCES, NTCES, and CIE chromaticity shift, and that the combination of these multimode thermometry techniques can be used for self-calibrating thermometry to improve accuracy.

4. Conclusion

In summary, a red emission double perovskite phosphor usable for three-mode optical thermometry is proposed. Heterovalent substitution of Sc^{3+} by Mg^{2+} causes contraction of the lattice to result in a significant increase in the oxygen vacancy content. The oxygen vacancy in turn induces intermediate states that enhance the upconversion luminescence intensity up to 4.32 times the original. The different responses of the red and two green emissions to temperature suits application for three-mode optical thermometry, based on the NTCES ($^2H_{11/2}$ and $^4F_{9/2}$) with $S_{r\text{-}max}$ up to 4.8% K^{-1} and δT as low as 0.016 K. The sample exhibits impressive relative sensitivity and superior signal resolution with good repeatability. Moreover, after approximately 100 000 evaluations with Python assistance, the difference between the predicted theoretical temperature and the actual test temperature remains within 6 K, which further demonstrates the reliability of this phosphor in practical applications. This work provides new insights for further enhancing UC luminescence intensity and the fabrication of high-performance multimode self-calibrating optical thermometry.

Data availability

The authors confirm that the data supporting the findings of this study are available within the article [and/or its ESI†].

Conflicts of interest

The authors declare no competing interests.

Acknowledgements

This work was supported by the Natural Science Foundation of Sichuan Province (Grant No. 2022NSFSC0362), and the Radiation Oncology Key Laboratory of Sichuan Province Open Fund (Grant No. 2023ROKF05). The authors would like to thank Ceshigo Research Service (https://www.ceshigo.com) for supporting the EPR test.

References

1 D. Parker, J. D. Fradgley and K.-L. Wong, The design of responsive luminescent lanthanide probes and sensors, *Chem. Soc. Rev.*, 2021, **50**, 8193–8213.
2 A. Bednarkiewicz, J. Drabik, K. Trejgis, D. Jaque, E. Ximendes and L. Marciniak, Luminescence based temperature bio-imaging: Status, challenges, and perspectives, *Appl. Phys. Rev.*, 2021, **8**, 011317.
3 H. Suo, X. Zhao, Z. Zhang, Y. Wang, J. Sun, M. Jin and C. Guo, Rational Design of Ratiometric Luminescence Thermometry Based on Thermally Coupled Levels for Bioapplications, *Laser Photonics Rev.*, 2021, **15**, 2000319.
4 H. Peng, M. I. J. Stich, J. Yu, L. Sun, L. H. Fischer and O. S. Wolfbeis, Luminescent Europium(III) Nanoparticles for Sensing and Imaging of Temperature in the Physiological Range, *Adv. Mater.*, 2010, **22**, 716–719.
5 X. Qiu, Q. Zhou, X. Zhu, Z. Wu, W. Feng and F. Li, Ratiometric upconversion nanothermometry with dual emission at the same wavelength decoded via a time-resolved technique, *Nat. Commun.*, 2020, **11**, 4.
6 L. Marciniak, K. Kniec, K. Elżbieciak-Piecka, K. Trejgis, J. Stefanska and M. Dramićanin, Luminescence thermometry with transition metal ions. A review, *Coord. Chem. Rev.*, 2022, **469**, 214671.
7 K. Li, Z. Zhang, D. Zhu and C. Yue, Excellent temperature sensitivities based on the FIR technique of up-conversion luminescence in a novel $NaLaTi_2O_6$:Yb^{3+},Tm^{3+} material, *Inorg. Chem. Front.*, 2024, **11**, 7464–7474.
8 A. M. Kaczmarek, M. Suta, H. Rijckaert, A. Abalymov, I. Van Driessche, A. G. Skirtach, A. Meijerink and P. Van Der Voort, Visible and NIR Upconverting Er^{3+} –Yb^{3+} Luminescent Nanorattles and Other Hybrid PMO–Inorganic Structures for In Vivo Nanothermometry, *Adv. Funct. Mater.*, 2020, **30**, 2003101.
9 L. Pu, P. Li, J. Zhao, Y. Wang, D. Guo, L. Li, Z. Wang and H. Suo, Eu^{3+}–Activated Single–Band Ratiometric Nanothermometry by Lattice Negative Thermal Expansion, *Laser Photonics Rev.*, 2023, **17**, 2200884.
10 M. Jia, X. Chen, R. Sun, D. Wu, X. Li, Z. Shi, G. Chen and C. Shan, Lanthanide-based ratiometric luminescence nanothermometry, *Nano Res.*, 2023, **16**, 2949–2967.
11 J. Liao, M. Wang, F. Lin, Z. Han, B. Fu, D. Tu, X. Chen, B. Qiu and H.-R. Wen, Thermally boosted upconversion and downshifting luminescence in $Sc_2(MoO_4)_3$:Yb/Er with two-dimensional negative thermal expansion, *Nat. Commun.*, 2022, **13**, 2090.
12 R. Song, R. Wang, X. Yang, X. Bian and H. Fu, Synergistic modulation of energy transfer and defect engineering toward anti-thermal quenching phosphor for high-sensitivity optical thermometry, *Appl. Mater. Today*, 2024, **38**, 102246.
13 R. Lu, X. Zhang, Y. Fang, X. Wu, M. Jia, K. Wang, J. Wu, Q. Li and Z. Sun, Europium Ions Self–Reduction Benefiting from AlO_4/Si(Al)O_4 Network Structure for Multimode Optical Thermometry Manometry, *Laser Photonics Rev.*, 2024, 2400409.
14 Z. Liao, B. Cao, L. Li, Y. Cong, Y. He and B. Dong, Exploring the excitation spectrum behavior of Dy in CaWO4 for a new excited-state-based ratiometric thermometry, *Appl. Mater. Today*, 2023, **31**, 101765.
15 J. Y. Chen, J. Q. Chen, L. J. Li, W. N. Zhang, L. P. Chen and H. Guo, A four-mode high-sensitive optical thermometer based on $Ca_3LiZnV_3O_{12}$:Sm^{3+} phosphors, *Mater. Today Chem.*, 2023, **29**, 101409.
16 S. Liu, L. Yan, J. Huang, Q. Zhang and B. Zhou, Controlling upconversion in emerging multilayer core–shell nanostructures: from fundamentals to frontier applications, *Chem. Soc. Rev.*, 2022, **51**, 1729–1765.
17 J. Zhou, Q. Liu, W. Feng, Y. Sun and F. Li, Upconversion Luminescent Materials: Advances and Applications, *Chem. Rev.*, 2015, **115**, 395–465.
18 X. Yang, R. Song, X. Gong, H. Deng, C. He, J. Liu, P. Zhou and H. Fu, Multi-shell structured nanomaterials with strong red upconversion emission for trimodal biomedical imaging, *Ceram. Int.*, 2024, **50**, 1601–1606.
19 X. Wang, R. R. Valiev, T. Y. Ohulchanskyy, H. Ågren, C. Yang and G. Chen, Dye-sensitized lanthanide-doped upconversion nanoparticles, *Chem. Soc. Rev.*, 2017, **46**, 4150–4167.
20 G. Li, S. Cheng, X. Chen, M. Wang, F. Zhang, Z. Chen, Y. Liang, X. Li, H. Ji, D. Yang, Y. Han, X. Li, W. Xu, M. Jia, C. Shan and Z. Shi, Erbium–Induced Boost in Self–Trapped Exciton Emission of Double Perovskites for Highly Sensitive Multimodal and Multiplexed Optical Thermography, *Adv. Funct. Mater.*, 2024, 2403073.
21 Y. Shi, X. Zhang, X. Wang and Y. Zhang, Pure Green Upconversion from a Multicolor Downshifting Perovskite Crystal, *Adv. Opt. Mater.*, 2023, **11**, 2202704.
22 Y. Wang, Q. Zhang, C. Yang and Z. Xia, Ratiometric Fluorescence Optical Fiber Enabling Operando

Temperature Monitoring in Pouch–Type Battery, *Adv. Mater.*, 2024, **36**, 2401057.

23 S. Heer, K. Kömpe, H.-U. Güdel and M. Haase, Highly Efficient Multicolour Upconversion Emission in Transparent Colloids of Lanthanide–Doped $NaYF_4$ Nanocrystals, *Adv. Mater.*, 2004, **16**, 2102–2105.

24 F. Wang and X. Liu, Upconversion Multicolor Fine-Tuning: Visible to Near-Infrared Emission from Lanthanide-Doped $NaYF_4$ Nanoparticles, *J. Am. Chem. Soc.*, 2008, **130**, 5642–5643.

25 A. Chauhan, S. Kataria, D. Busko, F. A. Cardona, A. Turshatov and B. S. Richards, Elucidating the role of metal-ion co-doping towards boosting upconversion luminescence in gadolinium vanadate, *J. Mater. Chem. C*, 2021, **9**, 16709–16720.

26 E. L. Cates, A. P. Wilkinson and J.-H. Kim, Delineating Mechanisms of Upconversion Enhancement by Li^+ Codoping in $Y_2SiO_5:Pr^{3+}$, *J. Phys. Chem. C*, 2012, **116**, 12772–12778.

27 M. Chen, L. Zeng, H. Zhou, J. Zeng, X. Wang, T. Pang, J. Tang and D. Chen, Enhanced upconversion luminescence in $LaVO_4:Yb^{3+}/Er^{3+}$ nanorods through Ba^{2+} ions doping, *Ceram. Int.*, 2023, **49**, 32000–32007.

28 Z. Huang, M. Yi, H. Gao, Z. Zhang and Y. Mao, Enhancing single red band upconversion luminescence of $KMnF_3$: Yb^{3+}/Er^{3+} nanocrystals by Mg^{2+} doping, *J. Alloys Compd.*, 2017, **694**, 241–245.

29 R. Wang, R. Song, C. Wang, T. Luo, J. Hu and H. Fu, Upconversion luminescence and temperature sensing performance of Zn^{2+}-doped Ba_2GdAlO_5: Yb^{3+}, Er^{3+} phosphors, *Ceram. Int.*, 2024, **50**, 21083–21091.

30 S. Du, F. Liu, H. Cao, Z. Mi and H. Huang, A giant enhancement in the up-conversion luminescence and high temperature sensitivity of Bi^{3+} doped $ZnMoO_4:Er^{3+}$ up-conversion phosphor, *Phys. Chem. Chem. Phys.*, 2022, **24**, 29909–29917.

31 H. Tan, Z. Zhao, W. Zhu, E. N. Coker, B. Li, M. Zheng, W. Yu, H. Fan and Z. Sun, Oxygen Vacancy Enhanced Photocatalytic Activity of Pervoskite $SrTiO_3$, *ACS Appl. Mater. Interfaces*, 2014, **6**, 19184–19190.

32 L. Luo, L. Fu, H. Liu, Y. Xu, J. Xing, C.-R. Chang, D.-Y. Yang and J. Tang, Synergy of Pd atoms and oxygen vacancies on In_2O_3 for methane conversion under visible light, *Nat. Commun.*, 2022, **13**, 2930.

33 Z. Zhao, Z. Wang, J. Zhang, C. Shao, K. Dai, K. Fan and C. Liang, Interfacial Chemical Bond and Oxygen Vacancy–Enhanced In_2O_3/CdSe–DETA S–scheme Heterojunction for Photocatalytic CO_2 Conversion, *Adv. Funct. Mater.*, 2023, **33**, 2214470.

34 L. Liang, X. Li, Y. Sun, Y. Tan, X. Jiao, H. Ju, Z. Qi, J. Zhu and Y. Xie, Infrared Light-Driven CO_2 Overall Splitting at Room Temperature, *Joule*, 2018, **2**, 1004–1016.

35 Y. Li, L. Yao, Z. Yin, Z. Cheng, S. Yang and Y. Zhang, Defect-induced abnormal enhanced upconversion luminescence in $BiOBr:Yb^{3+}/Er^{3+}$ ultrathin nanosheets and its influence on visible-NIR light photocatalysis, *Inorg. Chem. Front.*, 2020, **7**, 519–528.

36 S. Su, C. Hu, S. Ding, Y. Sun, L. Sun, Y. Zou, R. Liu, Z. Lei, B. Teng and D. Zhong, Achieving Broadband NIR Emission in Fe^{3+}–Activated $ALaBB'O_6$ (A = Ba, Sr, Ca; B–B′ = Li–Te, Mg–Sb) Phosphors via Multi–Site Ionic Co–Substitutions, *Adv. Opt. Mater.*, 2024, **12**, 2302383.

37 H. Dong, Z. Lei, S. Su, W. Yang, X. Zhang, W. Teng, G. Zu, B. Teng and D. Zhong, Achieving high-sensitivity dual-mode optical thermometry via phonon-assisted cross-relaxation in a double-perovskite structured up-conversion phosphor, *Inorg. Chem. Front.*, 2024, **11**, 2784–2797.

38 H. Zhang, Y. Liang, H. Yang, S. Liu, H. Li, Y. Gong, Y. Chen and G. Li, Highly Sensitive Dual-Mode Optical Thermometry in Double-Perovskite Oxides via Pr^{3+}/Dy^{3+} Energy Transfer, *Inorg. Chem.*, 2020, **59**, 14337–14346.

39 R. D. Shannon, Revised effective ionic radii and systematic studies of interatomic distances in halides and chalcogenides, *Acta Crystallogr., Sect. A*, 1976, **32**, 751–767.

40 R. Song, H. Li, H. Zhang, H. Tang, X. Tang, J. Yang, H. Zhao and J. Zhu, Tunable luminescence and improved thermostability via Tm–Dy energy transfer in a tellurooxyphosphate phosphor, *Appl. Mater. Today*, 2023, **30**, 101712.

41 X. Bian, R. Wang, S. Li, Q. Shi and H. Fu, Dual anti-thermal quenching induced by defect levels of the $Ba_3EuAl_2O_{7.5}$ phosphor, *J. Lumin.*, 2023, **257**, 119768.

42 R. Song, Z. Zhang, H. Li, Z. Luo, J. Yang, J. Ma, X. Xiang, Q. Zeng and J. Zhu, A single-phase white-emitting $La(BO_3, PO_4):Dy^{3+}$ phosphor with high thermostability, *Ceram. Int.*, 2023, **49**, 6965–6973.

43 R. Song, Y. Zheng, H. Li, Y. Mao, K. Xiong and J. Zhu, Charge compensation and solid-state lighting application for dysprosium-activated $Ba_2TeP_2O_9$ phosphor, *J. Alloys Compd.*, 2022, **912**, 165188.

44 R. Song, Z. Yang, H. Zhang, X. Tang, Y. Liu and J. Zhu, Highly thermally stable and tunable luminescence in microwave-assisted synthesized $Na_3Ca_4(TeO_3)(PO_4)_3:Dy^{3+}$, Eu^{3+} for ultra-high color rendering white light-emitting diodes, *Ceram. Int.*, 2023, **49**, 22323–22331.

45 K. Ye, K. Li, Y. Lu, Z. Guo, N. Ni, H. Liu, Y. Huang, H. Ji and P. Wang, An overview of advanced methods for the characterization of oxygen vacancies in materials, *TrAC, Trends Anal. Chem.*, 2019, **116**, 102–108.

46 S. Wang, H. Shi, S. Liang, H. Li, Y. Xia, R. Shao, T. Li, J. Shi, X. Wu and Z. Xu, Oxygen Vacancy and Bandgap Simultaneous Modulation to Achieve High Lithiophilicity and Mechanical Strength of Lithium Metal Anodes, *Small*, 2024, 2311740.

47 K. Lai, Y. Sun, H. Chen, L. Zhi and W. Wei, Effect of oxygen vacancy and Al-doping on the electronic and optical properties in SnO2, *Phys. B*, 2013, **428**, 48–52.

48 J. Zhu, T. Yang, H. Li, Y. Xiang, R. Song, H. Zhang and B. Wang, Improving the up/down-conversion luminescence via cationic substitution and dual-functional temperature sensing properties of Er^{3+} doped double perovskites, *Chem. Eng. J.*, 2023, **471**, 144550.

49 A. M. Kaczmarek, M. Suta, H. Rijckaert, T. P. van Swieten, I. Van Driessche, M. K. Kaczmarek and A. Meijerink, High temperature (nano)thermometers based on $LiLuF_4$:Er^{3+}, Yb^{3+} nano- and microcrystals. Confounded results for core–shell nanocrystals, *J. Mater. Chem. C*, 2021, **9**, 3589–3600.

50 Y. Chen, J. Chen, Y. Tong, W. Zhang, X. Peng, H. Guo and D. Huang, Y_4GeO_8:Er^{3+},Yb^{3+} up-conversion phosphors for optical temperature sensor based on FIR technique, *J. Rare Earths*, 2021, **39**, 1512–1519.

51 Y. Jiang, Y. Tong, S. Chen, W. Zhang, F. Hu, R. Wei and H. Guo, A three-mode self-referenced optical thermometry based on up-conversion luminescence of Ca_2MgWO_6:Er^{3+}, Yb^{3+} phosphors, *Chem. Eng. J.*, 2021, **413**, 127470.

52 M. Lin, L. Xie, Z. Wang, B. S. Richards, G. Gao and J. Zhong, Facile synthesis of mono-disperse sub-20 nm $NaY(WO_4)_2$:Er^{3+},Yb^{3+} upconversion nanoparticles: a new choice for nanothermometry, *J. Mater. Chem. C*, 2019, **7**, 2971–2977.

53 B. Dong, R. N. Hua, B. S. Cao, Z. P. Li, Y. Y. He, Z. Y. Zhang and O. S. Wolfbeis, Size dependence of the upconverted luminescence of $NaYF_4$:Er,Yb microspheres for use in ratiometric thermometry, *Phys. Chem. Chem. Phys.*, 2014, **16**, 20009.

54 Z. Rao, Z. Li, X. Zhao and X. Gong, Targeted high-precision up-converting thermometer platform over multiple temperature zones with Er^{3+}, *Mater. Horiz.*, 2023, **10**, 1816–1824.

55 G. Xiang, M. Xiong, Z. Yang, Y. Wang, L. Yao, S. Jiang, X. Zhou, L. Li, X. Wang and J. Zhang, Multipath optical thermometry realized by electronic levels and Stark sublevels of Er^{3+}, *Ceram. Int.*, 2024, **50**, 5261–5266.

56 Z. Gao, B. Tian, M. Liu, L. Yang, F. Shang and G. Chen, Luminescence and temperature-dependent sensitivity of Yb^{3+}/Er^{3+} doped glass ceramics containing $NaGd(MoO_4)_2$ nanocrystals, *J. Non-Cryst. Solids*, 2023, **603**, 122114.

57 F. Luo, J. Xing, Y. Qin, Y. Zhong, F. Shang and G. Chen, Up-conversion luminescence, temperature sensitive and energy storage performance of lead-free transparent Yb^{3+}/Er^{3+} co-doped $Ba_2NaNb_5O_{15}$ glass-ceramics, *J. Alloys Compd.*, 2022, **910**, 164859.

58 Y. Zhang, X. Chai, J. Li, X. Wang, Y. Li and X. Yao, Enhanced up-conversion luminescence and excellent temperature sensing properties in Yb^{3+} sensitized Er^{3+}-doped $Bi_3Ti_{1.5}W_{0.5}O_9$ multifunctional ferroelectric ceramics, *J. Alloys Compd.*, 2018, **735**, 473–479.

59 C. Hernández-Álvarez, P. I. Martín-Hernández, I. R. Martín, F. Rivera-López, H. Hemmerich, J. Llanos and M. Runowski, Monitoring of the heating rate of a motorized gear system using UV-curable resin containing Y_2WO_6:Yb^{3+}-Er^{3+} up-converting nanoparticles as optical temperature sensor, *Appl. Mater. Today*, 2024, **38**, 102207.

60 K. Saidi and M. Dammak, Upconversion luminescence and optical temperature sensing characteristics of Er^{3+}/Yb^{3+} codoped $Na_3Gd(PO_4)_2$ phosphors, *J. Solid State Chem.*, 2021, **300**, 122214.

61 J. Chen, W. Zhang, S. Cui, X. Peng, F. Hu, R. Wei, H. Guo and D. Huang, Up-conversion luminescence properties and temperature sensing performances of $Ba_5Y_8Zn_4O_{21}$:Yb^{3+}, Er^{3+} phosphors, *J. Alloys Compd.*, 2021, **875**, 159922.

62 X. Chen, Y. Zhang, Y. Bu, Y. Chen, Y. Chen, J. Fu, J. Li and D. Deng, A multi-mode optical thermometer based on the up-conversion $Ca_3Y_2Ge_3O_{12}$: Er^{3+}, Yb^{3+} phosphor, *J. Lumin.*, 2023, **261**, 119907.

63 L. Li, Y. Tong, J. Chen, Y. Chen, G. Abbas Ashraf, L. Chen, T. Pang and H. Guo, Up–conversion and temperature sensing properties of $Na_2GdMg_2(VO_4)_3$:Yb^{3+},Er^{3+} phosphors, *J. Am. Ceram. Soc.*, 2022, **105**, 384–391.

64 H. Lv, L. Luo, W. Li and P. Du, Manipulating Upconversion Emission and Thermochromic Properties of Ho^{3+}/Yb^{3+}-Codoped $Al_2Mo_3O_{12}$ Microparticles by Negative Lattice Expansion for Multimode Visual Optical Thermometry, *Inorg. Chem.*, 2022, **61**, 11442–11453.

65 W. Piotrowski, K. Trejgis, K. Maciejewska, K. Ledwa, B. Fond and L. Marciniak, Thermochromic Luminescent Nanomaterials Based on Mn^{4+}/Tb^{3+} Codoping for Temperature Imaging with Digital Cameras, *ACS Appl. Mater. Interfaces*, 2020, **12**, 44039–44048.

66 J. Xue, Z. Yu, H. M. Noh, B. R. Lee, B. C. Choi, S. H. Park, J. H. Jeong, P. Du and M. Song, Designing multi-mode optical thermometers via the thermochromic $LaNbO_4$:Bi^{3+}/Ln^{3+} (Ln = Eu, Tb, Dy, Sm) phosphors, *Chem. Eng. J.*, 2021, **415**, 128977.

